

Nonlinear vibrations of thin plates with variable thickness: Application to sound synthesis of cymbals

Quoc Bao Nguyen^{a)} and Cyril Touzé^{b)}

IMSIA, ENSTA ParisTech-CNRS-EDF-CEA, Université Paris Saclay, 828 Boulevard des Maréchaux, 91762 Palaiseau Cedex, France

(Received 7 November 2018; revised 20 January 2019; accepted 29 January 2019; published online 22 February 2019)

Geometrically nonlinear vibrations of thin plates and shells with variable thickness are investigated numerically with the purpose of synthesizing the sound of cymbals. In cymbal making, taper refers to the gradual change in thickness from the centre to the rim and is known to be a key feature that determines the tone of the instrument. It is generally used in conjunction with shape variations in order to enable the cymbal to play a bell-like sound when hit near its centre, or a crash sound when struck close to the edge. The von Kármán equations for thin plates with thickness and shape variations are derived, and a numerical method combining a Rayleigh-Ritz approach together with a Störmer-Verlet scheme for advancing the problem in time is detailed. One main advantage of the method is its ability to implement easily any frequency-dependent loss mechanism which is a key property for sound synthesis. Also, the accuracy of the computation of the nonlinear restoring force is especially preserved. The method is employed to synthesize the sounds of cymbal-like instruments. The impact of taper is addressed and the relative effects of both thickness and shape variations, are contrasted. © 2019 Acoustical Society of America. <https://doi.org/10.1121/1.5091013>

[AM]

Pages: 977–988

I. INTRODUCTION

Cymbals belong to the category of percussion instruments having a long history, and used in various contexts, from orchestral symphonic music to pop-rock and jazz music.^{1,2} Having different shapes, names and tones and a wide range of playability, sounds, and colors, they serve as the basis of all drum kits in modern amplified music, jazz bands, and percussion ensembles. The usual terminologies to designate their roles and sounds are known as: *ride*, *splash*, and *crash*; the last two names of which are evidently onomatopoeic. Ride cymbals are the largest ones, generally used to play a steady rhythmic pattern, whereas crash and splash are smaller and used to play dramatic accents.

In cymbal making, taper refers to the thickness variation encountered from the centre to the edge of a cymbal. Indeed, for most of the cymbals, taper is very important in order to confer the cymbals the ability to have two distinct tones. On the one hand, cymbals shall play a clear tone with a dominant pitch when hit near the centre, in the region known as the bell. This bell-like sound is essential to mark the beat and is favoured by two different physical characteristics: the protruding dome manufactured at centre, and the thickness which is more important in this area. On the other hand, a non-tonal, bright glittering sound is awaited when strongly striking crash and splash cymbals at the edge.

A series of measurements have been realized in two different drum stores in Paris with an electronic vernier calliper in order to quantify more precisely the thickness at centre and

edge. It has been found that for crash cymbals, the thickness at edge h_e ranges from 0.9 to 0.5 mm, the minimal values being obtained for series known for their explosive sounds: The Paiste fast crash 14 in. (35 cm diameter) and the Sabian AA thin crash (30 cm diameter), and also for the Paiste “paperthin formula 602,” generally used in hi-hat. The mean measured value for crash is 0.65–0.7 mm. The thickness at centre h_c is larger, with measured values ranging from 1.4 to 0.9 mm. For ride cymbals, h_c can go up to 1.5 mm, while h_e ranges between 1.4 and 0.8 mm. Splash cymbals are the smallest ones, and h_e has been found to be on the order of 0.55–0.65 mm, with a minimal value $h_e = 0.4$ mm for a Sabian AAX splash 8 in. (20 cm diameter).

The bright shimmering sound of gongs and cymbals is obtained thanks to strongly nonlinear vibrations^{1,3} occurring because the amplitude of the vibrations is larger than the thickness. Recent studies revealed that the phenomenon at hand is wave turbulence, resulting from the geometric nonlinearity, and also at work in gongs and thunder plates.^{4–8} For the gongs, the energy cascade driven by the wave turbulence can be relatively slow and take up to half a second to fully develop and attain the highest frequencies. This results in the characteristic sound of gongs with a blow-up of higher frequencies occurring shortly after the strike. In the case of cymbals (and more specifically for crash and splash), taper strongly favours the nonlinearity by reducing the thickness close to the edge. Consequently, the cascade of energy and the excitation of high frequencies is very fast, so that the maximal frequency is obtained right after the strike, without an audible delay.

Numerical simulations and sound synthesis based on physical models face a number of difficulties while solving for the vibrations, the nonlinearity and the presence of the

^{a)}Also at: Laboratoire Modélisation et Simulation Multi Echelle (MSME), CNRS - UPEC - UPEM, Marne-la-Vallée, France.

^{b)}Electronic mail: cyril.touze@ensta-paristech.fr

wave turbulence effect being the most important ones. However, successful results have been obtained in the last years, where a key component has been the derivation of energy-conserving schemes for von Kármán problems describing geometrically nonlinear vibrations of thin plates.^{9,10} The temporal scheme has then been used together with finite difference methods,¹¹ or with a modal approach,⁴ the advantage of which is to offer an ability to easily implement losses with any frequency-dependent law, and to give a better control on the accuracy of the computation of the nonlinear terms. These two points are key to ensuring the realism of synthesized sounds. Other methods have been used where the kinematics of plates and shells is simplified by using ad-hoc bending models that are easier to implement for finite element approaches, hence opening the doors to create more complex geometries for a wide variety of shells.¹² This last work has been more deeply investigated recently,¹³ with an interesting improvement to efficiently simulate the energy cascade due to wave turbulence thanks to the phenomenological model proposed by Humbert *et al.*¹⁴

Even though the sound of gongs has been recovered with accuracy and realism by using the modal approach,⁴ simulations of cymbal-like circular plates failed to reproduce the very fast cascade and the immediate emergence of the broadband Fourier spectrum, which gives crash and splash cymbals their specific sparkling and explosive sound. More specifically, simulations with a constant and very small thickness, on the order of 0.5 mm, even though showing an immediate energy blow-up, depart from the sound of cymbals as showing a too important pitch glide and a sound that tends to resemble that of a thin sheet of metal, and not a cymbal. A main reason is the absence of taper in earlier simulations, thus not covering the ability of cymbals to play two different sounds when hit near the centre or close to the edge. Rigidifying the centre of the structure maintains a satisfactory global bending stiffness while having a thinner edge where the nonlinearity can express more easily to develop the high-frequency content of the spectrum very rapidly. The goal of this article is thus to introduce a nonlinear model for plate vibrations including both taper (thickness variations) and curvature (also denoted as bow in cymbal description terminology, i.e., shape variations), and to develop a numerical method for solving the problem in time, based on earlier works.^{4,15–17} Once the model is established, numerical simulations are drawn in order to show the important effect of taper on the nonlinear vibrations, and to contrast both effects of shape and thickness variations as well as to distinguish the bell sound from the crash sound obtained with strikes at the edge.

II. MODEL AND METHODS

In this section, the equations of motion for a thin plate with variable thickness are first recalled. A linear analysis is then performed for the two unknowns, namely the transverse displacement w and the Airy stress function F . The problem is subsequently discretized using a Rayleigh-Ritz approach and the time integration method is detailed. Finally, a complete model including thickness together with shape

variations, modeled as an imperfection of the plate at rest, is highlighted.

A. von Kármán model for thin plates with variable thickness

In this paper, a circular plate of radius R_d , made of a homogeneous material of volume density ρ , Young's modulus E , and Poisson's ratio ν is considered. The surface of the plate is denoted as $\mathcal{S} = \{(r, \theta) \in [0, R_d] \times [0, 2\pi]\}$. In order to simplify the presentation, the thickness of the plate h is assumed to depend only on the radius coordinate r . The von Kármán model for geometrically nonlinear vibrations of thin plates is used to compute the solutions for the transverse displacement $w(r, \theta, t)$ and the Airy stress function $F(r, \theta, t)$. It reads^{18–21}

$$\begin{aligned} \rho h(r)\ddot{w} + \Delta(D(r)\Delta w) - (1 - \nu)\mathcal{L}(D(r), w) \\ = p(r, \theta, t) - R(\dot{w}) + \mathcal{L}(w, F), \end{aligned} \quad (1a)$$

$$\Delta(B(r)\Delta F) - (1 + \nu)\mathcal{L}(B(r), F) = -\frac{1}{2}\mathcal{L}(w, w). \quad (1b)$$

In these expressions, $D(r) = Eh^3(r)/12(1 - \nu^2)$ is the flexural rigidity, $B(r) = 1/Eh(r)$, p stands for the normal pressure loading, and $R(\dot{w})$ is a generic expression accounting for the losses. Δ is the Laplacian operator, and \mathcal{L} is the von Kármán bilinear operator, which reads, in polar coordinates for two arbitrary functions $f(r, \theta)$ and $g(r, \theta)$

$$\begin{aligned} \mathcal{L}(f, g) = f_{,rr} \left(\frac{g_r}{r} + \frac{g_{,00}}{r^2} \right) + g_{,rr} \left(\frac{f_r}{r} + \frac{f_{,00}}{r^2} \right) \\ - 2 \left(\frac{f_{,r\theta}}{r} + \frac{f_{,\theta}}{r^2} \right) \left(\frac{g_{,r\theta}}{r} + \frac{g_{,\theta}}{r^2} \right). \end{aligned} \quad (2)$$

As compared to the equations of motion with constant thickness,¹⁶ the main incidence of the variable thickness onto the equations of motion is an added complexity to derive the linear terms. On the other hand, the nonlinear terms are not affected by the thickness variations, which is in line with the definition of the geometric nonlinearity. As applications to cymbals are targeted, a free-edge boundary condition is selected. It reads,¹⁶ $\forall t, \forall \theta \in [0, 2\pi]$, and for $r = R_d$

$$w_{,rr} + \frac{\nu}{R_d} w_{,r} + \frac{\nu}{R_d^2} w_{,\theta\theta} = 0, \quad (3a)$$

$$w_{,rrr} + \frac{1}{R_d} w_{,rr} - \frac{1}{R_d^2} w_{,r} + \frac{2 - \nu}{R_d^2} w_{,r\theta\theta} - \frac{3 - \nu}{R_d^3} w_{,\theta\theta} = 0, \quad (3b)$$

$$F_{,r} + \frac{1}{R_d} F_{,\theta\theta} = 0, \quad F_{,r\theta} + \frac{1}{R_d} F_{,\theta} = 0. \quad (3c)$$

B. Linear analysis

The aim of this section is to analyse the linear part of Eqs. (1). As already underlined, the linear terms are deeply modified when taking the variable thickness into account,

hence most of the added work focuses on calculating these new terms. In the course of this section, the results will be derived without referring to a particular case of boundary conditions, for the sake of generality. However, when turning to numerical results, the free-edge boundary condition presented in Sec. II A, is used. The linear parts of Eqs. (1a) and (1b) correspond to two distinct linear problems in terms of the two unknowns w and F , respectively. Each of these two problems is tackled separately by using the Rayleigh-Ritz method with the appropriate boundary conditions.

1. Transverse vibration

The linear solution for the transverse vibration is first derived. The problem at hand reads

$$\rho h(r)\ddot{w} + \Delta(D(r)\Delta w) - (1 - \nu)\mathcal{L}(D(r), w) = 0. \quad (4)$$

Let us assume that the eigenmodes of this problem with constant thickness [i.e., a perfect flat plate with h_0 a reference thickness, and $D(h_0)$ its flexural rigidity] are known and denoted as $\Phi_p(r, \theta)$ for the eigenfunctions and ω_p for the eigenfrequencies, meaning that we have

$$\Delta\Delta\Phi_p(r, \theta) = \frac{\rho h_0}{D(h_0)} \omega_p^2 \Phi_p(r, \theta). \quad (5)$$

In the computations, h_0 is defined from the thickness variation profile as the value at the plate centre. The eigenfunctions $\Phi_p(r, \theta)$ verify the boundary conditions for the transverse displacement w at the edge, and they are assumed to be normalized such that $\int_S \Phi_p \Phi_q dS = \delta_{pq}$, with δ_{pq} the Kronecker symbol. Following the Rayleigh-Ritz approach, the problem in Eq. (4) is discretized in space with the expansion $w(r, \theta) = \sum^{N_\Phi} X_p(t) \Phi_p(r, \theta)$. Substituting this last expression in Eq. (4), multiplying by another basis function Φ_j and integrating over the surface S , the problem can be rewritten as

$$\mathbf{M}_\Phi \ddot{\mathbf{X}} + \mathbf{K}_\Phi \mathbf{X} = \mathbf{0}, \quad (6)$$

with $\mathbf{X} = [X_1, X_2, \dots, X_{N_\Phi}]^T$ being the vector of generalized coordinates and N_Φ the number of transverse modes retained in the truncation. The complete expressions for the mass and stiffness matrices \mathbf{M}_Φ and \mathbf{K}_Φ are given in Appendix A. The advantage of using the Rayleigh-Ritz method in the case of a circular plate where the modes of the perfect plate $\Phi_p(x)$ are analytic is that the resulting coefficients appearing in \mathbf{M}_Φ and \mathbf{K}_Φ can be obtained with a better accuracy and convergence control than those computed with more numerically-oriented methods, such as the finite-difference scheme where the convergence is more difficult to be achieved up to high frequencies.²¹

2. Airy stress function

The same methodology is applied to the second linear Eq. (1b), which reads

$$\Delta(B(r)\Delta F) - (1 + \nu)\mathcal{L}(B(r), F) = 0. \quad (7)$$

This problem in case of constant thickness is associated with in-plane eigenmodes Ψ_j , which verify $\Delta\Delta\Psi_j = \zeta_j^4 \Psi_j$, together with the associated boundary conditions. Expanding the unknown $F(r, \theta) = \sum^{N_\Psi} Y_p \Psi_p(r, \theta)$, the Rayleigh-Ritz approach applied to Eq. (7) leads to

$$\mathbf{K}_\Psi \mathbf{Y} = \mathbf{0}, \quad (8)$$

with $\mathbf{Y} = [Y_1, Y_2, \dots, Y_{N_\Psi}]^T$ the vector of generalized coordinates and N_Ψ the number of in-plane modes retained in the truncation. Note that no mass matrix is present here as the longitudinal inertia is neglected in the von Kármán model. The complete expressions of the entries of \mathbf{K}_Ψ are given in Appendix B.

3. Comparison with a finite element computation

In order to validate eigenmode computation with the Rayleigh-Ritz method, a comparison is drawn with the results obtained from a commercial finite element (FE) software, namely ANSYS. The case study is that of a free edge circular plate, with radius $R_d = 0.2$ m, and material parameters as $E = 2.10^{11}$ Pa, $\nu = 0.38$, and $\rho = 7860$ kg/m³. Two thickness variations are selected and represented in Figs. 1(a) and 1(b). In the first case, the thickness is constant and equal to 1 mm from the centre to $r = 0.04$ m, then it decreases linearly from that point to the edge, with a final value at edge h_e , which is a parameter ranging from $h_e = 1$ mm (case of a plate with constant thickness) to $h_e = 0.4$ mm. In the second case shown in Eq. 1(b), a parabolic dependence of the thickness on the radius is selected, with the same range of variation for the thickness at edge h_e . In this numerical test, only the transverse eigenfrequencies corresponding to Eq. (6) can be easily computed as no direct output relative to the in-plane problem can be found. However, since the coding of the two problems share numerous similarities, it has been found sufficient to test only the transverse problem. In the Rayleigh-Ritz method, the convergence is controlled by the number of modes N_Φ used as a projection space to build the matrices \mathbf{M}_Φ and \mathbf{K}_Φ . It has been found that $N_\Phi = 150$ was sufficient to obtain converged values for the first 31 eigenfrequencies shown in Figs. 1(c) and 1(d). Note that the first 31 eigenmodes includes 28 asymmetric modes (having equal eigenfrequencies as being degenerate) and three axisymmetric modes, consequently Fig. 1 shows only 17 frequencies.

Regarding the computations realised with ANSYS, the FE solution has been obtained by using the element SHELL181, a four-node element with six degrees of freedom at each node implementing a Reissner-Mindlin kinematics. These computations have reached a fine convergence by using up to 33 387 nodes (33 091 elements).

Figures 1(c) and 1(d) show the results obtained by varying h_e . When $h_e = 1$ mm, the thickness is uniform, and one retrieves the eigenfrequencies of a perfect circular plate. Decreasing h_e leads to the reduction of the local stiffness of the plate, so that the eigenfrequencies are also lessened, explaining the general trend observed on the curves. Finally, one observes a very good match between the eigenfrequencies calculated with the two methods. Whereas the results

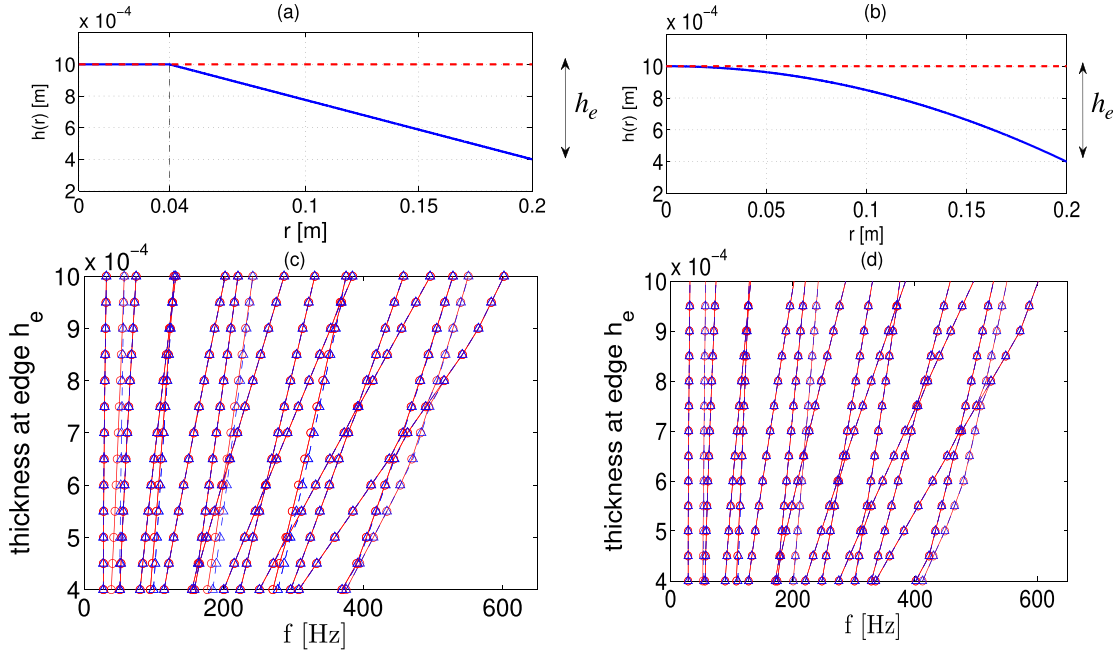


FIG. 1. (Color online) Comparison of eigenfrequency computation for two different cases of thickness variation. (a) Thickness constant near centre then linearly decreasing. (b) Parabolic thickness. (c)–(d) Eigenfrequency variations for $h_e \in [0.4, 1]$ mm, corresponding respectively to cases (a) and (b). Red circles: Rayleigh-Ritz method, Blue triangles: Finite-element model.

are perfectly similar in the case 2 (parabolic variation of thickness), case 1 (linear variation with two different slopes) shows some slight discrepancies between the two methods. They are attributed to the modeling difference and in particular to the fact that transverse shear is taken into account in the FE model.

C. Nonlinear analysis and time integration

We now address the time integration of the full problem given by Eqs. (1), including the nonlinear terms and the losses. Following the Rayleigh-Ritz procedure started in Sec. II B to solve the linear part, i.e., using the expansions $w(r, \theta) = \sum^{N_\Phi} X_p(t) \Phi_p(r, \theta)$ and $F(r, \theta) = \sum^{N_\Psi} Y_j(t) \Psi_j(r, \theta)$, one can rewrite Eqs. (1) as

$$\mathbf{M}_\Phi \ddot{\mathbf{X}} + \mathbf{K}_\Phi \mathbf{X} + \mathbf{C}_\Phi \dot{\mathbf{X}} = \mathbf{N}_\Phi(\mathbf{X}, \mathbf{Y}) + \mathbf{P}_f, \quad (9a)$$

$$\mathbf{K}_\Psi \mathbf{Y} = -\frac{1}{2} \mathbf{N}_\Psi(\mathbf{X}, \mathbf{X}). \quad (9b)$$

Note that, as underlined before, the thickness variation modifies only the linear parts of the von Kármán equations of motion. Consequently, in the semi-discrete equations [Eqs. (9)], the new terms appearing are: the force vector \mathbf{P}_f , of which the entry k reads: $\mathbf{P}_{fk} = \int_S p(r, \theta, t) \Phi_k(r, \theta) dS, \forall k \in [0, N_\Phi]$; the damping matrix \mathbf{C}_Φ which will be detailed later, and the two quadratic nonlinear terms $\mathbf{N}_\Phi(\mathbf{X}, \mathbf{Y})$ and $\mathbf{N}_\Psi(\mathbf{X}, \mathbf{X})$. These two nonlinear terms are computed following earlier studies on plates with uniform thickness, see, e.g., Refs. 4, 16, and 19. They are two vectors with the entry k reading as

$$\mathbf{N}_\Phi(\mathbf{X}, \mathbf{Y})_k = \sum_{i=1}^{N_\Phi} \sum_{j=1}^{N_\Psi} E_{ij}^k X_i Y_j, \quad (10a)$$

$$\mathbf{N}_\Psi(\mathbf{X}, \mathbf{X})_k = \sum_{p=1}^{N_\Phi} \sum_{q=1}^{N_\Phi} H_{pq}^k X_p X_q, \quad (10b)$$

where the introduced coefficients E_{ij}^k and H_{pq}^k write

$$E_{ij}^k = \int_S \Phi_k \mathcal{L}(\Phi_i, \Psi_j) dS, \quad (11a)$$

$$H_{pq}^k = \int_S \Psi_k \mathcal{L}(\Phi_p, \Phi_q) dS. \quad (11b)$$

Note that Eqs. (9) can be condensed by replacing Eq. (9b) into Eq. (9a), highlighting the fact that a cubic nonlinearity is at hand for the transverse displacement variable \mathbf{X} . Also, the von Kármán operator \mathcal{L} has some symmetry properties,¹⁹ such that for some particular boundary conditions, the relationship $E_{m,n}^l = H_{m,l}^n$ is fulfilled.⁴ The free-edge boundary conditions considered in this paper belong to the category where the relationship holds, so that subsequent gain in pre-computing time can be saved thanks to this symmetry property.

The damping matrix \mathbf{C}_Φ has to be populated with ad-hoc values. As underlined in Ref. 4, one advantage of the present approach is that one can select modal damping factors at ease, following any frequency dependence. However, as the problem is semi-discretized by using the eigenmodes of the plate with constant thickness that are not the eigenmodes of the problem considered, the relationship between the modal damping matrix $\mathbf{C} = \text{diag}(\mu_k)$ (with $\mu_k = 2\xi_k \omega_k$ the modal loss coefficient associated to the modal loss factor ξ_k) and \mathbf{C}_Φ has to be used. Even though the equations of motion will be integrated in time using Eqs. (9), the idea is to use the modal loss coefficients μ_k as input parameters of the simulations, since the physical meaning of these values is more

tractable. Then, using \mathbf{P} the matrix of normalized eigenvectors computed from Eq. (6), the matrix \mathbf{C}_Φ is computed using the relationship $\mathbf{C} = \mathbf{P}^T \mathbf{C}_\Phi \mathbf{P}$.

To integrate the problem in time, a Störmer-Verlet scheme is used. This is a symmetric and symplectic method of order two.²² It is simply deduced from Eqs. (9) by replacing the second-order time derivative by the centred finite difference operator $\delta_{tt} \equiv 1/k^2(e_{t+} - 2 + e_{t-})$, where k is the time step, and e_{t+} and e_{t-} are, respectively, the forward and backward shift operators. The first-order time derivative for the damping term is replaced by the centred finite difference operator $\delta_t \equiv 1/2k(e_{t+} - e_{t-})$, and all the other terms are computed at the current time step. The method has a linear stability condition reading $f_S > \pi f_{N_\Phi}$, with $f_S = 1/k$ is the sampling rate and f_{N_Φ} the eigenfrequency of the last transverse mode retained in the truncation.

D. A complete model with shape imperfection

A complete model for the simulation of cymbal vibrations can be derived from the previous one by adding a static, geometric imperfection to the plate model, representing the position of the structure at rest. Let us denote this geometric imperfection $w_0(r, \theta)$. In order to comply with von Kármán assumptions,^{17,19} w_0 should not be too large so as to obtain a shallow shell. The full model equations can be derived easily following for example,^{15,23} and read

$$\begin{aligned} \rho h(r) \ddot{w} + \Delta(D(r) \Delta w) - (1 - \nu) \mathcal{L}(D(r), w) \\ = \mathcal{L}(w, F) + \mathcal{L}(w_0, F) + p - R(\dot{w}), \end{aligned} \quad (12a)$$

$$\begin{aligned} \Delta(B(r) \Delta F) - (1 + \nu) \mathcal{L}(B(r), F) \\ = -\frac{1}{2} [\mathcal{L}(w, w) + 2\mathcal{L}(w, w_0)]. \end{aligned} \quad (12b)$$

Note that taking this shape imperfection into account modifies only the nonlinear terms appearing in the right-hand side. The complete model can be semi-discretized in the same manner, following the Rayleigh-Ritz method and using the eigenmodes of the perfect plate without imperfection nor thickness variation as the expansion basis. The shape imperfection w_0 has also to be expanded as¹⁵

$$w_0(r, \theta) = \sum_{k=1}^{N_k} a_k \Phi_k(r, \theta) + z_g, \quad (13)$$

where z_g is the centre of mass offset due to imperfection, and the coefficients a_k are the semi-discrete representation of the shape. They read

$$a_k = \int_S (w_0 - z_g) \Phi_k dS, \quad (14)$$

$$z_g = \frac{\int_S w_0 dS}{A_p}, \quad (15)$$

where A_p is the area of the perfect plate. The two unknowns w and F are expanded using the same

procedure as in Sec. II C. This leads to a semi-discrete problem reading

$$\mathbf{M}_\Phi \ddot{\mathbf{X}} + \mathbf{K}_\Phi \mathbf{X} + \mathbf{C}_\Phi \dot{\mathbf{X}} = \mathbf{N}_\Phi(\mathbf{X}, \mathbf{Y}) + \mathbf{N}_\Phi(\mathbf{a}, \mathbf{Y}) + \mathbf{P}f, \quad (16a)$$

$$\mathbf{K}_\Psi \mathbf{Y} = -\frac{1}{2} [\mathbf{N}_\Psi(\mathbf{X}, \mathbf{X}) + 2\mathbf{N}_\Psi(\mathbf{a}, \mathbf{X})]. \quad (16b)$$

In these equations, the nonlinear terms \mathbf{N}_Φ and \mathbf{N}_Ψ have the same expressions as in Eqs. (10), the only difference being that they are also applied to the imperfection represented by the vector $\mathbf{a} = [a_1, a_2, \dots, a_{N_\Phi}]^T$. Consequently, the \mathbf{Y} vector, linked to the Airy stress function, is a function with linear and quadratic dependence on \mathbf{X} . Substituting Eqs. (16b) into (16a), one observes now that the problem from the transverse motion arising from the right-hand side of Eq. (16a) shows a linear, quadratic, and cubic dependence on \mathbf{X} . The linear dependence can be solved alone so as to obtain the eigenmodes and eigenfrequencies of the complete problem. All these computations closely follow those presented by Camier *et al.*,¹⁵ where only the shape imperfection was taken into account. The method was compared to finite element simulations to assess the results, and this step has been repeated here, showing a perfect agreement. Finally, to integrate the semi-discrete problem in time, the Störmer-Verlet scheme is used, as in Sec. II C.

III. NUMERICAL SIMULATIONS

A. Effect of variable thickness

Numerical simulations are conducted to highlight the effect of the thickness variation on the nonlinear vibrations of circular plates, and in particular on the explosiveness of the cymbal sound at the very beginning of a strong hit. Indeed, cymbals are known to produce on a very short time scale a very rich spectrum with a broadband frequency content, which is typical of their bright shimmering sound. In order to quantify the effect of thickness variations, a circular plate of radius $R_d = 0.2$ m has been selected, with material parameters typical for a metallic alloy: Young's modulus $E = 2.10^{11}$ Pa, Poisson's ratio $\nu = 0.38$, and mass density $\rho = 7860$ kg.m⁻³. The thickness variation has been selected with a constant thickness $h_0 = 1$ mm, for $r \in [0, 0.05]$ m, and then a linear decrease to a value h_e at $r = R_d$. Two cases, namely, $h_e = 0.7$ mm and $h_e = 0.4$ mm, are investigated and compared to the plate with uniform thickness h_0 . These two cases have been selected from the thickness measurements realized on a number of cymbals: while $h_e = 0.7$ mm corresponds to a mean value found for crash cymbals, $h_e = 0.4$ mm is taken as the minimal thickness that can be reasonably attained and which has been measured on a splash cymbal. The modal damping coefficients have been selected following the rule: $\mu_k = 0.007 \omega_k^{0.6} + 2$. The constant term entails a small constant amount of damping even for the very low frequency modes, while the power-law form has already been used in Ref. 4; it is based on measured experimental values identified in very large thin plates²⁴ and

has been found to give realistic results for the sound synthesis of gongs.

To assess the explosiveness of the sound, a strike is given as an input force to the plate. This strike is located at a given point $\mathbf{x}_0 = (r_0, \theta_0)$ so that $p(r, \theta, t) = \delta(\mathbf{x} - \mathbf{x}_0)g(t)$, and the temporal content is a raised cosine:

$$g(t) = \begin{cases} \frac{p_m}{2} [1 + \cos(\pi(t - t_0)/T_{wid})] & \text{if } |t - t_0| \leq T_{wid}; \\ 0 & \text{if } |t - t_0| > T_{wid}. \end{cases} \quad (17)$$

The input parameters of the force are thus the time t_0 , the temporal width of the interaction T_{wid} , and the amplitude of the force p_m in N. All the computations have been implemented using the software *VK-GONG*,²⁵ an open source code developed to handle nonlinear vibrations of plates and built from previous works by the second author. The first eigenfrequency of the plate with constant thickness $h_0 = 1$ mm is equal to 32 Hz, while the 800th transverse mode frequency is 18 861 Hz. Consequently, all the calculations have been performed with $N_\Phi = 800$ so as to ensure an almost complete covering of the frequency band of human hearing. For the number of in-plane modes, $N_\varphi = 60$ has been selected following the convergence guidelines given by Ducceschi *et al.*⁴ Note that this number is given as the cardinal of the subset of in-plane modes having non-vanishing coupling terms. This is another advantage of the method used to compute the coupling coefficients, especially for the case of free-edge circular plates where the modes are analytic and vanishing coefficients can be predicted from analytical formulas resulting in significant computational time savings. The sampling rate f_S has to be larger than 59 kHz in order to comply with the stability condition for the Störmer-Verlet scheme, *i.e.*, $f_S > \pi f_{N_\Phi}$ with $N_\Phi = 800$. For all the computations, the sampling rate has been selected as $f_S = 100$ kHz, well over the stability limit.

A first set of simulations is realized with an amplitude of the strike as $p_m = 90$ N located at the edge of the

plate ($r_0 = R_d$), and a short interaction time selected as $T_{wid} = 1$ ms in order to mimick a strong hit given by a drumstick. Figure 2 shows the results obtained for the three cases investigated: the uniform plate, and the two plates with variable thickness, respectively, with $h_e = 0.7$ mm and $h_e = 0.4$ mm. The first row, Figs. 2(a)–2(c), shows the displacement at an arbitrary point located at $r = 0.1792$ m (close to the edge), and $\theta = 0.52$ rad, while the second row presents the spectrograms of the velocity of the same output point. The effect of the thickness variation is huge and can be clearly assessed both on the temporal displacement signal and the velocity spectrogram. For the displacement, one can observe that for the plate with uniform thickness, the maximum value of the displacement is reached at the beginning and is equal to 2 mm, while for $h_e = 0.7$ mm, the maximum is 3 mm and finally 4 mm for the thinnest plate with $h_e = 0.4$ mm. One can also remark that the global decay of the vibration appears to be clearly exponential for the uniform thickness, showing that from $t = 0.6$ s to the end, the linear terms—and more specifically the losses—control the dynamics. On the other hand, nonlinearities are much more important for the two other cases with a more pronounced high-frequency content and a different decay.

The fast spectral enrichment can be more evidently assessed with the velocity spectrograms shown in Figs. 2(d)–2(f). For the plate with uniform thickness, most of the energy is concentrated below 5000 Hz, while the rapid generation of high frequencies is much more pronounced for the two cases with thickness variations. In particular, when $h_e = 0.4$ mm, frequencies up to 15 kHz are created in the very first milliseconds of the vibration. This results in a more explosive sound which is typical for a cymbal, while the sound produced by the plate with uniform thickness has not the same properties. The readers are invited to hear at the associated sound files, corresponding to the velocity resampled at 44.1 kHz, which are available as supplementary materials.²⁶ Note that all the sounds corresponding to the simulations presented in the figures are available as WAV

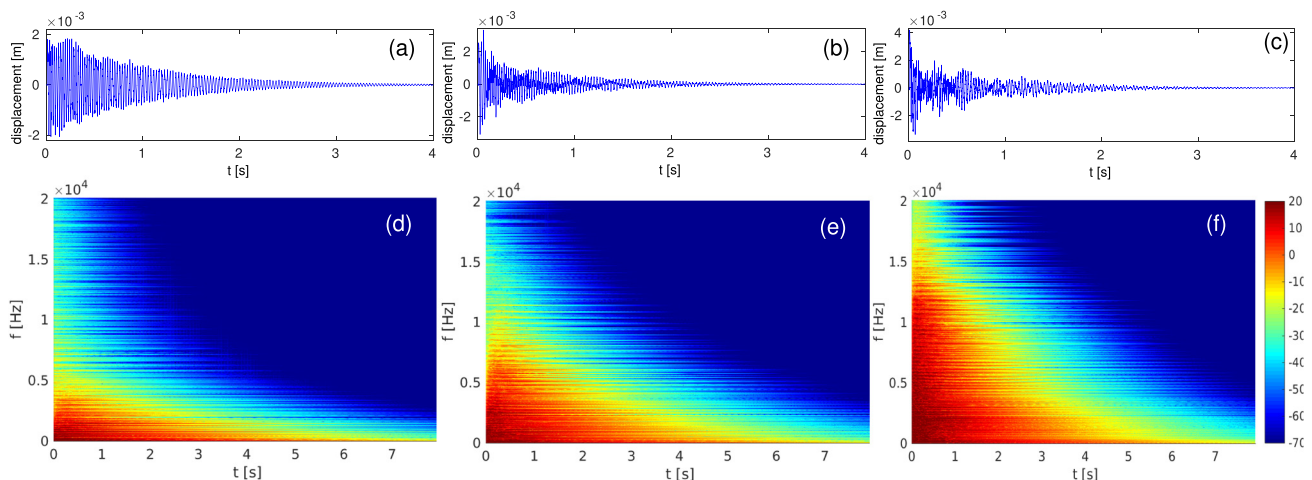


FIG. 2. (Color online) Output displacements [first row, (a)–(c)] and velocity spectrograms [second row, (d)–(f)] for the simulations of the nonlinear vibrations of a thin circular plate with a uniform thickness $h = 1$ mm (a), (d); with a linearly varying thickness down to $h_e = 0.7$ mm (b), (e), and to $h_e = 0.4$ mm (c), (f). Displacement of an arbitrary point located at $r = 0.1792$ m, and spectrogram of the velocity derived from the same displacement signal, in dB with a 90 dB dynamic.

files. To complete the comparisons, a WAV file corresponding to the case of a thin plate with uniform thickness $h=0.4\text{ mm}$ is also provided, so that the reader could hear how a uniform but too small thickness degrades the quality of the sound synthesized, enhancing the pitch glide and departing the sound produced from that of a real cymbal.

Figure 3 compares the displacement field of the plates with uniform thickness 1 mm (left column) to that obtained with the variable thickness and $h_e=0.4\text{ mm}$ at different instants. For these figures, the amplitude of the excitation force p_m has been raised to 150 N in order to enhance the vibration amplitudes. The temporal width of the strike is

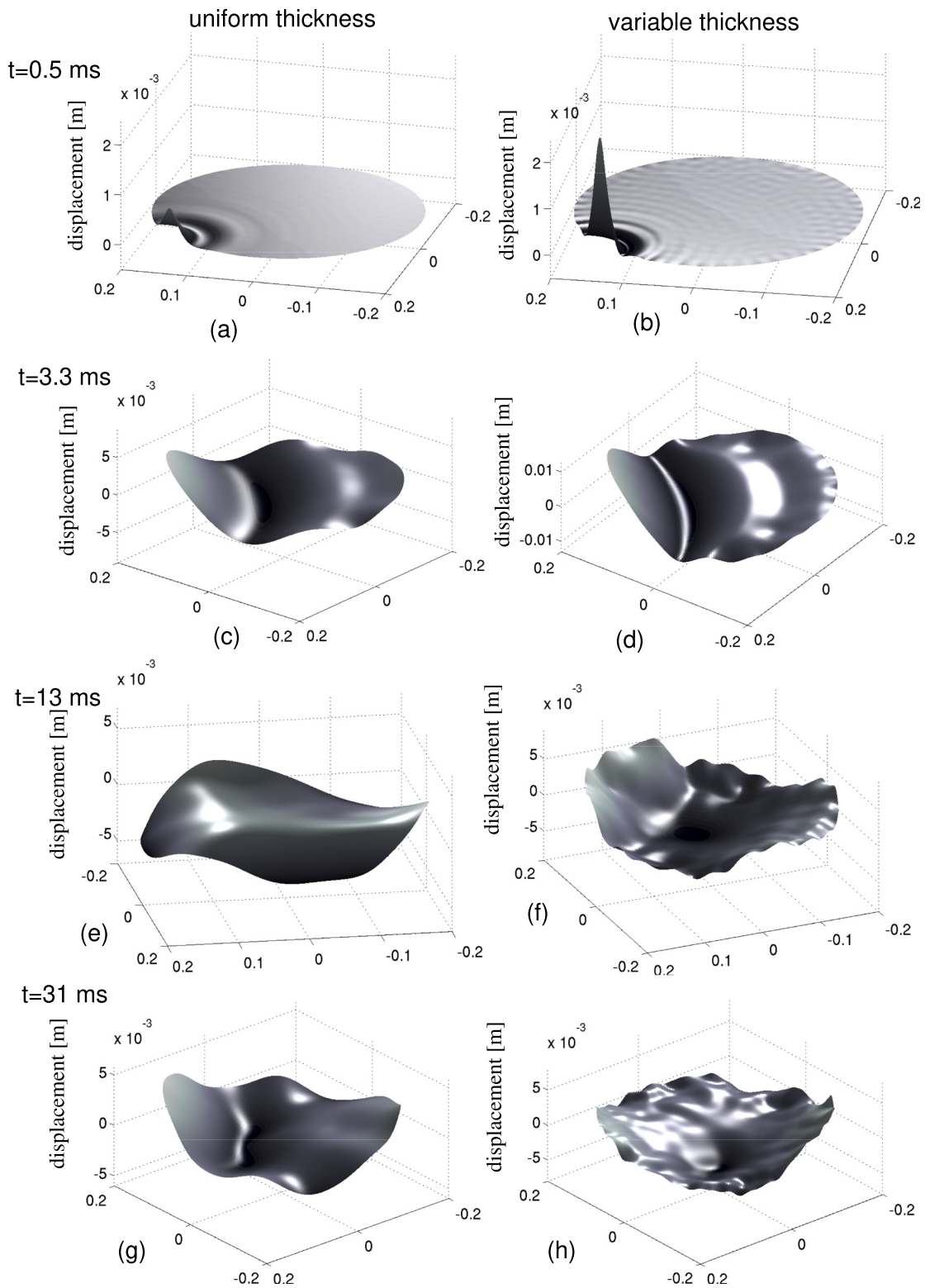


FIG. 3. (Color online) Snapshots of the displacement fields. Comparison between the plate with uniform thickness $h_0 = 1\text{ mm}$ [left column, (a), (c), (e), (g)] and the plate with thickness at edge $h_e = 0.4\text{ mm}$ [right column, (b), (d), (f), (h)], and at four different instants: $t = 0.5\text{ ms}$ (a), (b), $t = 3.3\text{ ms}$ (c), (d), $t = 13\text{ ms}$ (e), (f), and $t = 31\text{ ms}$ (g), (h). Strike imposed at the edge at $t = 0$, with an amplitude $p_m = 150\text{ N}$.

kept as $T_{wid} = 1$ ms, which means that, according to the raised cosine formula in Eq. (17), the input force lasts from $t = 0$ to 3 ms. The first row shows the displacement field just after the beginning of the strike, at $t = 0.5$ ms. One can see that the difference in the local stiffness between the two plates (local thickness 1 mm vs 0.4 mm), gives rise to very distinct magnitudes of displacements at the striking point (0.5 mm for the uniform thickness vs 2.2 mm). The second row shows the displacement fields at $t = 3.3$ ms, i.e., right after the end of the input striking force. One can clearly observe that the plate with variable thickness experiences much more high frequencies, as attested by the important wavelets localized on the opposite side of the striking point. The last two rows present the displacement fields at $t = 13$ and 31 ms, showing undoubtedly how the high frequency content is very quickly excited in the vibration and localized in the regions of smaller thickness. The last two rows clearly evidenced the very nonlinear characteristics of the vibration field when the thickness of the plate is severely decreased, as compared to the case of the constant thickness.

In order to have more quantitative results on the high-frequency content generated by the vibration, the following characteristic frequency f_c is introduced as

$$f_c = \frac{\int_{f=0}^{f_s/2} a(f)^2 f df}{\int_{f=0}^{f_s/2} a(f)^2 df}, \quad (18)$$

where $a(f)$ is the Fourier amplitude (evaluated at frequency f) of the velocity signal obtained from the output point at $r = 0.1792$ m, and $f_s = 100$ kHz is the sampling rate. This characteristic frequency has already been used for quantifying the frequency content of a turbulent cascade of energy,²⁷ as well as for the energy transfer observed in the contact dynamics of strings against frets.²⁸ Figure 4 shows the behaviour of this characteristic frequency as function of the

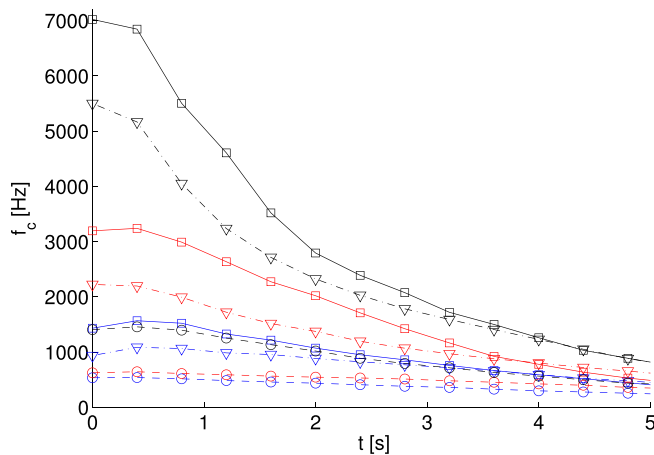


FIG. 4. (Color online) Characteristic frequency f_c defined in Eq. (18) as a function of the time t of the computed velocities. Blue lines correspond to the case of the plate with uniform thickness $h = 1$ mm, red lines to the plate with linear varying thickness and $h_e = 0.7$ mm, and black lines with $h_e = 0.4$ mm. Three different strike amplitudes are used for each case: $p_m = 20$ N (circles \circ), 90 N (triangles ∇), and 150 N (squares \square).

time t of the computed velocity output, and for nine simulations, with three different plates (uniform thickness, $h_e = 0.7$ mm and $h_e = 0.4$ mm) and three different striking amplitudes ($p_m = 20, 90,$ and 150 N); thus giving a quantitative point of view to the frequency behaviours displayed by the spectrograms shown in Figs. 2(d)–2(f). In particular, one can clearly see the considerable effect of decreasing the thickness at edge from 1 to 0.4 mm, as the characteristic frequency is almost equal in the cases $h_e = 1$ mm, $p_m = 150$ N and $h_e = 0.4$ mm, and $p_m = 20$ N. Concentrating on the case $p_m = 150$ N, one can observe that the characteristic frequency is multiplied by a factor of 2 when h_e is decreased from 1 to 0.7 mm, and once again a factor of 2.3 by decreasing from 0.7 to 0.4 mm.

B. A complete model for cymbal vibrations

In this section, a complete model including both shape and thickness variations, is considered. The shape of the imperfection has been measured on a real Zildjian “custom rock” crash cymbal having a radius $R_d = 0.2$ m, and shown in Fig. 5. The height at the centre H_c has been found equal to 3.4 cm; however, it will be used as a free parameter in order to compare cymbals with different shallowness. In particular, simulations with $H_c = 1.7$ cm (half of the real measurement, shown as a dashed line in Fig. 5), will be addressed.

The main aim of the section is to compare the relative effects of shape and thickness variations on the sound produced by cymbals, and in particular the ability of producing two distinctive sounds when hit on the bell or at the edge.

A first comparison is drawn out in Fig. 6, which shows the velocity spectrograms of two different cases simulated. The first case, Fig. 6(a), is that of a plate having uniform thickness $h = 1$ mm, and only shape variation following the profile shown in Fig. 5 with a maximum height at centre $H_c = 3.4$ cm. In the second case, the same shape variation is considered, and a thickness dependence following the guidelines used in Sec. III A is taken into account: a linear thickness variation with $h_e = 0.4$ mm. The two velocity spectrograms shown in Fig. 6 are thus complementary to those shown in Fig. 2 and must be compared altogether. In particular, contrasting Fig. 6(a) with 2(d), i.e., the two cases with the uniform thickness $h = 1$ mm and with/without shape variations, one can observe that the energy transfer is slightly more pronounced in the case with shape variation. Indeed, the maximum frequency attained in the spectrogram of Fig. 6(a) is around 750–800 Hz, whereas it is only 500 Hz in Fig. 2(d) for the flat plate. This phenomenon is easily

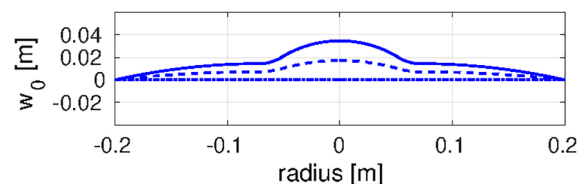


FIG. 5. (Color online) Profile of the shape imperfection used in the simulations. The shape has been measured from a real cymbal, with a height at centre $H_c = 3.4$ cm. An intermediate case with $H_c = 1.7$ cm (dashed line), is also considered.

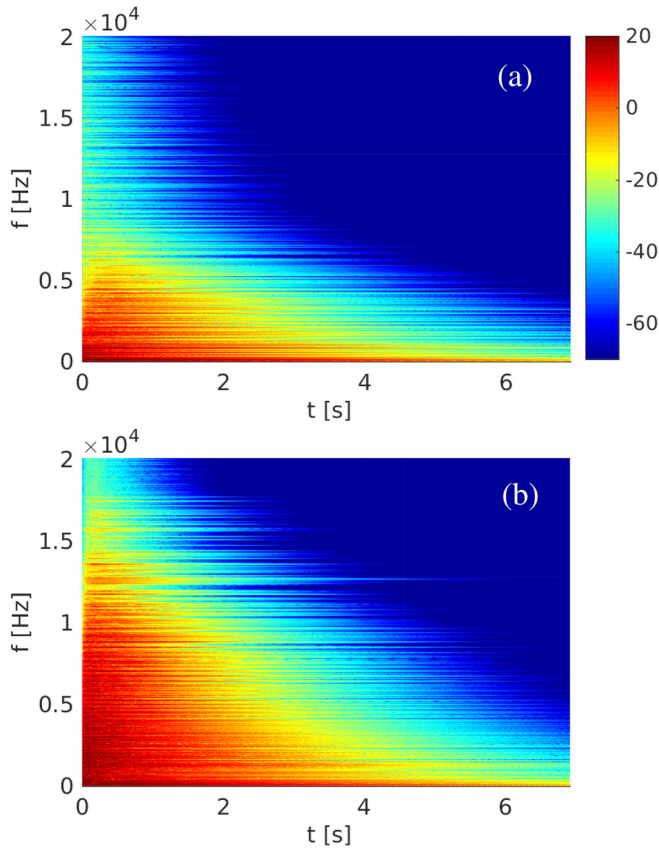


FIG. 6. (Color online) Spectrogram of velocity with a 90 dB range. Strike at $t = 0$ s, with amplitude $p_m = 90$ N, and contact time $T_{wid} = 1$ ms. (a) cymbal with uniform thickness $h = 1$ mm, shape variation only with height at centre $H_c = 3.4$ cm. (b) cymbal with the same shape variation, $H_c = 3.4$ cm, and linear decrease of the thickness, $h_e = 0.4$ mm.

explained by the presence of quadratic nonlinearity in the case of shape imperfections, which is key to generating more easily energy transfers.²⁹ This effect is aurally particularly striking (see companion wav files): the enrichment brought by the shape and the quadratic nonlinearities is really noticeable, especially because it happens in the most sensitive frequency band for the ear. However, shape variation alone is not sufficient in order to create a rich spectrum as that obtained in Fig. 2(f). Adding the thickness variation allows retrieving the bright spectrum with frequencies up to 14 kHz, as shown in Fig. 6(b). Hence, variation of thickness seems to be really needed in order to build the explosive sound and excite very high frequencies beyond 10 kHz; however, it is undoubted that shape variation is already important and adds a brightness to the sound produced by adding frequencies in the sensitive band of the ear.

For a more quantitative comparison, Fig. 7 shows the characteristic frequencies for a number of test cases, mixing both shape and thickness variations. Interestingly, it is found that when the thickness is uniform, $h = 1$ mm, and with the maximum height of the shape imperfection being half the measured one, $H_c = 1.7$ cm; a better energy build-up is obtained than with $H_c = 3.4$ cm. This can be explained that this case offers a better compromise between the appearance of quadratic nonlinearity and the stiffening effect produced by the curvature. Increasing H_c results in a more and more

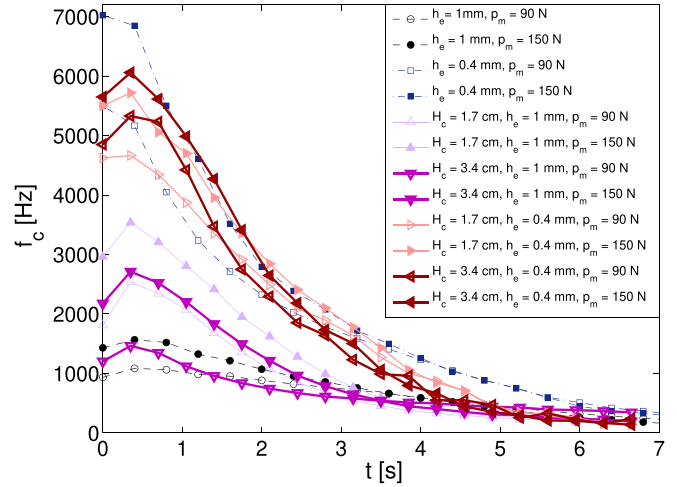


FIG. 7. (Color online) Characteristic frequency f_c as a function of the time t for 12 different cases reported in inset, mixing shape, and thickness variations, amplitudes of strike at the edge 90, and 150 N.

stiff structure with increasing eigenfrequencies, making the couplings between modes and energy transfer more difficult. Anyhow, Fig. 7 highlights that adding a shape imperfection always favours the energy build-up, but the thickness variation is also needed in order to attain very high values for this characteristic frequency. Indeed, all the curves with $h_e = 0.4$ mm are always the upper one for the characteristic frequency f_c .

Another aspect not investigated yet with the thickness decrease is related to the pitch glide. Indeed, decreasing the thickness at the edge results in geometric nonlinearities more easily excited since they are proportional to the ratio between the transverse displacement and the thickness. The pitch glide is related to the backbone curve of the modes of the structure, and is more pronounced if the transverse displacement is large as compared to h .^{3,11,30–32} A problem one may encounter if the plate is too thin, is that the pitch glide will be too important, resulting in a sound which is not pleasant to the ear and will more resemble that of a membrane. This effect can be easily simulated with the methods used in this paper, showing the need to stiffen the structure and explaining why very thin flat plates are not used as cymbals. This is illustrated in Fig. 8(a) concerning the case of the plate with linear thickness variation and $h_e = 0.4$ mm for a vigorous strike with $p_m = 150$ N. The attention is paid to the low frequency range, below 1200 Hz, and the very important pitch glides of all frequency peaks are clearly visible. On the other hand, Fig. 8(b) is concerned with a cymbal with uniform thickness and shape variation only, with a maximum height at centre $H_c = 3.4$ cm. In this case, the cymbal is so stiff that almost no pitch glide is present, even though an important strike is given to the structure. Figure 8(c) displays the case with $h_e = 0.4$ mm and $H_c = 3.4$ cm, where a good compromise is found between creating a strong nonlinear effect resulting in rapid energy build-up, and minimizing the pitch glide which shall not be too pronounced and unpleasant to the ear.

The last simulation investigates the behaviour of the cymbal when hit at centre. Indeed, as stated before, a bell

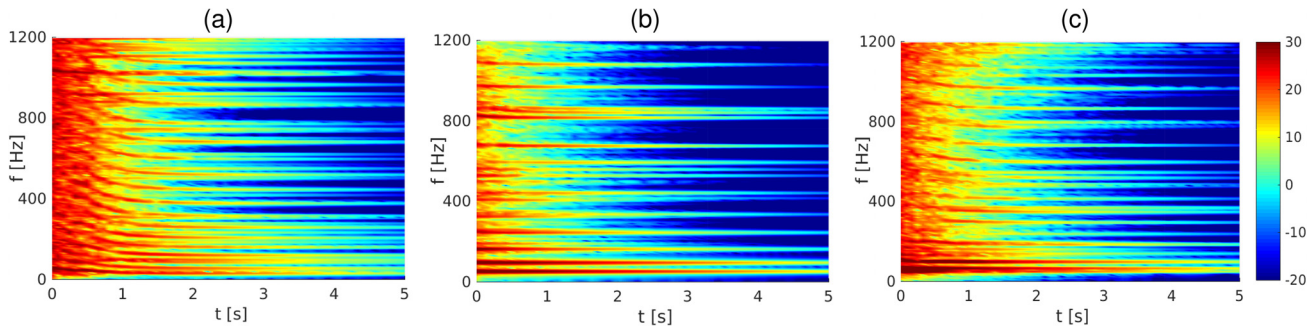


FIG. 8. (Color online) Velocity spectrograms in the low frequency range for a strike at the edge of magnitude $p_m = 150$ N, and for three different cymbal configurations. Restrained range of 50 dB in order to highlight the frequency peaks. (a) Only linear thickness variation down to $h_e = 0.4$ mm, flat plate without shape imperfection. (b) Shape variation only with height at centre $H_c = 3.4$ cm, and uniform thickness $h = 1$ mm. (c) Shape and thickness variation with $H_c = 3.4$ cm and $h_e = 0.4$ mm.

sound has to be obtained when striking the cymbal near the centre. Figure 9 shows the velocity spectrograms for three different cymbal configurations and two amplitudes of strikes, $p_m = 20$ N and $p_m = 90$ N. The strike is imposed near the centre, at $r = 4$ cm. Figures 9(a) and 9(b) consider the case of only thickness variation, with linear variation and $h_e = 0.4$ mm. It shows that even with moderate strikes, the nonlinear regime is too rapidly excited, and the broadband spectrum is at hand, even though the cymbal is hit at centre. This shows undoubtedly that this configuration is not stiff enough and cannot be used for a cymbal since the two distinctive sounds (bell and crash) are out of reach. Figures 9(c) and 9(d) show the results when only shape variation is considered, with $H_c = 3.4$ cm, and a constant thickness $h = 1$ mm. In this case, the spectrograms are almost unchanged and the sounds are completely equivalent to the ear. This is always the case if the strike is increased up to $p_m = 150$ N, meaning that linear vibrations are at hand up to very large amplitudes of input forces. This case appears to be too stiff, preventing the drummer from giving

some colours to the sound found when striking the bell. Finally, Figs. 9(e) and 9(f) show the results obtained with both shape and thickness variations, where $H_c = 3.4$ cm and $h_e = 0.4$ mm. This case seems to show a correct compromise, the sound produced when striking at centre being almost linear with a small excitation of nonlinearity for $p_m = 90$ N, giving a nice colour to the sound.

IV. CONCLUSION

This paper investigates the nonlinear vibrations of cymbals with a particular emphasis on the presence of the thickness variations in a physical model. While the model of flat plates with uniform thickness derived has been shown to be effective for simulating the sound of gongs,⁴ the explosive sound of cymbal was more difficult to obtain. Indeed, thickness and shape variations play important roles in cymbal making, particularly in order to obtain two different behaviours when the excitation is at the centre or at the edge. When a

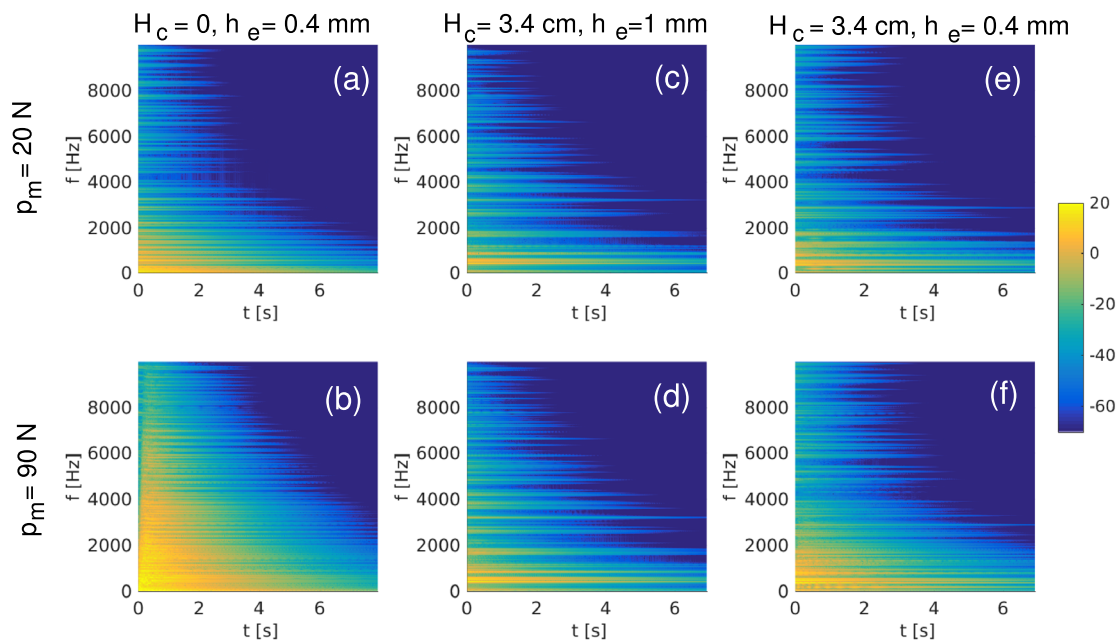


FIG. 9. (Color online) Velocity spectrograms, cymbal hit at $r = 4$ cm from the centre. First row: soft strike, $p_m = 20$ N, second row, hard strike, $p_m = 90$ N. First column (a)–(b): variable thickness only, $h_e = 0.4$ mm. Second column, (c)–(d): Shape variation only, uniform thickness $h = 1$ mm and height at centre $H_c = 3.4$ cm. Third column (e)–(f): $H_c = 3.4$ cm and linear thickness variation down to $h_e = 0.4$ mm.

cymbal is hit at its centre, a bell-like sound is awaited so that nonlinearities should not be too much excited. On the contrary, a scintillating sound with a rapid build-up of energy and generation of a large broadband Fourier spectrum in the first milliseconds is expected from vigorous strikes at the edge. One of the main outcomes of the present study is to derive such a model based on the von Kármán assumptions for thin plates, and accounting for both effects of thickness and shape variations. An ad-hoc numerical method is adopted, from earlier studies, to handle the complexity brought by these new terms for a time-domain simulation using the Störmer-Verlet scheme for time integration and the Rayleigh-Ritz method, which allows one to give frequency-dependent modal damping factors as inputs. The substantial effect of thickness variations has been underlined and a set of simulations has been conducted in order to get a comprehensive view of the two different effects, resulting from shape and thickness variations. Simulations and synthesized sounds show that shape variations are very important in creating higher frequencies more easily in the energy build-up, a result that was not expected but could easily be understood thanks to the quadratic nonlinearity. However, imposing only shape variations results in too stiff cymbals, so that only linear behaviour is observed when hit at the centre and the energy build-up is less important than that obtained with thickness variations. On the other hand, thickness variations alone make the plate too compliant in general, causing too high pitch glides that are not pleasant to the ear. Both of the physical features are thus needed, but the fact that shape variations already have an important effect, which is especially prominent in the frequency band where the ear is the most sensitive, shows that the thickness variations may be at a moderate level, a conclusion that is confirmed by the values of the edge thickness found in most of the cymbals.

APPENDIX A: LINEAR ANALYSIS FOR THE TRANSVERSE PROBLEM

In this section, the complete formula for computing the mass and stiffness matrices \mathbf{M}_Φ and \mathbf{K}_Φ , related to the linear problem for the transverse vibrations, are given. The mass matrix comes from the inertia term in Eq. (4). A simple calculation shows that the entries $M_{\Phi ij}$ read

$$\mathbf{M}_{\Phi ij} = \int_S \rho h(r) \Phi_i \Phi_j r dr d\theta. \quad (\text{A1})$$

In order to easily compute the current term in the stiffness matrix, the following identity is used:

$$\Delta(D(r)\Delta\Phi_p) = \Delta D \Delta\Phi_p + D \Delta \Delta\Phi_p + 2\nabla D \cdot \nabla(\Delta\Phi_p). \quad (\text{A2})$$

Consequently, the stiffness matrix can be decomposed as $\mathbf{K}_\Phi = \mathbf{K}_\Phi^1 + \mathbf{K}_\Phi^2 + \mathbf{K}_\Phi^3 + \mathbf{K}_\Phi^4$, where the entries of each term read

$$\mathbf{K}_{\Phi ij}^1 = \int_S (\Delta D)(\Delta\Phi_j) \Phi_i r dr d\theta, \quad (\text{A3})$$

$$\mathbf{K}_{\Phi ij}^2 = \int_S \omega_j^2 D(r) \Phi_i \Phi_j r dr d\theta, \quad (\text{A4})$$

$$\mathbf{K}_{\Phi ij}^3 = 2 \int_S \nabla D \cdot \nabla(\Delta\Phi_j) \Phi_i r dr d\theta, \quad (\text{A5})$$

$$\mathbf{K}_{\Phi ij}^4 = -(1 - \nu) \int_S \mathcal{L}(D, \Phi_j) \Phi_i r dr d\theta. \quad (\text{A6})$$

These equations can be used for an arbitrary boundary condition once the eigenmodes Φ_i and eigenfrequencies ω_i are known. In the case of a free edge, the eigenmodes write $\Phi_{kn}(r, \theta) = R_{kn}(r) \cos k\theta$ (first configuration) and $\Phi_{kn}(r, \theta) = R_{kn}(r) \sin k\theta$ (second configuration), where the index k refers to the number of nodal diameters and n to the number of nodal circles. When $k=0$, the modes are axisymmetric and no dependence on θ is found. When $k \neq 0$, the eigenfrequency is degenerated with a multiplicity of 2, and the two configurations, one in sine and the other one in cosine, are present. $R_{kn}(r)$ is a combination of Bessel functions, the expression of which is given by Touzé *et al.*¹⁶ Plugging these expressions of Φ_i into the previous equations, one can separate the radial part from the angular part, and all the expressions are analytic. The integrals are then computed numerically from the analytic expressions, leading to a perfect control of the accuracy of the results.

APPENDIX B: LINEAR ANALYSIS FOR THE IN-PLANE PROBLEM

Using the same identity [Eq. (A2)] to develop the terms arising from Eq. (7), one can write $\mathbf{K}_\Psi = \mathbf{K}_\Psi^1 + \mathbf{K}_\Psi^2 + \mathbf{K}_\Psi^3 + \mathbf{K}_\Psi^4$, where the elements of each matrix read

$$\mathbf{K}_{\Psi ij}^1 = \int_S \Delta B \Delta\Psi_j \Psi_i r dr d\theta, \quad (\text{B1})$$

$$\mathbf{K}_{\Psi ij}^2 = \int_S \zeta_j^4 D(r) \Psi_j \Psi_i r dr d\theta, \quad (\text{B2})$$

$$\mathbf{K}_{\Psi ij}^3 = 2 \int_S \nabla B \cdot \nabla(\Delta\Psi_j) \Psi_i r dr d\theta, \quad (\text{B3})$$

$$\mathbf{K}_{\Psi ij}^4 = -(1 + \nu) \int_S \mathcal{L}(B, \Psi_j) \Psi_i r dr d\theta. \quad (\text{B4})$$

¹N. H. Fletcher and T. D. Rossing, *The Physics of Musical Instruments*, 2nd ed. (Springer, New York, 1998).

²T. D. Rossing and R. J. Weiss, *Science of Percussion Instruments* (World Scientific, Singapore, 2000).

³A. Chaigne, C. Touzé, and O. Thomas, "Nonlinear vibrations and chaos in gongs and cymbals," *Acoust. Sci. Technol. Acoust. Soc. Jpn.* **26**(5), 403–409 (2005).

⁴M. Ducceschi and C. Touzé, "Modal approach for nonlinear vibrations of damped impacted plates: Application to sound synthesis of gongs and cymbals," *J. Sound Vib.* **344**, 313–331 (2015).

⁵C. Touzé, S. Bilbao, and O. Cadot, "Transition scenario to turbulence in thin vibrating plates," *J. Sound Vib.* **331**(2), 412–433 (2012).

⁶G. Düring, C. Josserand, and S. Rica, "Weak turbulence for a vibrating plate: Can one hear a Kolmogorov spectrum?," *Phys. Rev. Lett.* **97**, 025503 (2006).

⁷A. Boudaoud, O. Cadot, B. Odille, and C. Touzé, "Observation of wave turbulence in vibrating plates," *Phys. Rev. Lett.* **100**, 234504 (2008).

- ⁸O. Cadot, M. Ducceschi, T. Humbert, B. Miquel, N. Mordant, C. Josserand, and C. Touzé, “Wave turbulence in vibrating plates,” in *Handbook of Applications of Chaos Theory*, edited by C. Skiadas (Chapman and Hall/CRC Press, London, 2016), pp. 425–448.
- ⁹S. Bilbao, “A family of conservative finite difference schemes for the dynamical von Kármán plate equations,” *Numer. Methods Partial Diff. Eq.* **24**(1), 193–216 (2007).
- ¹⁰S. Bilbao, O. Thomas, C. Touzé, and M. Ducceschi, “Conservative numerical methods for the full von Kármán plate equations,” *Numer. Methods Partial Diff. Eq.* **31**(6), 1948–1970 (2015).
- ¹¹S. Bilbao, “Percussion synthesis based on models of nonlinear shell vibration,” *IEEE Trans. Audio Speech Lang. Process.* **18**(4), 872–880 (2010).
- ¹²J. N. Chadwick, S. S. An, and D. L. James, “Harmonic shells: A practical nonlinear sound model for near-rigid thin shells,” *ACM Trans. Graphics* **28**(5), 119 (2009).
- ¹³G. Cirio, A. Qu, G. Drettakis, E. Grinspun, and C. Zheng, “Multi-scale simulation of nonlinear thin-shell sound with wave turbulence,” *ACM Trans. Graphics* **37**(4), 110 (2018).
- ¹⁴T. Humbert, C. Josserand, C. Touzé, and O. Cadot, “Phenomenological model for predicting stationary and non-stationary spectra of wave turbulence in vibrating plates,” *Phys. D: Nonlinear Phenom.* **316**, 34–42 (2016).
- ¹⁵C. Camier, C. Touzé, and O. Thomas, “Non-linear vibrations of imperfect free-edge circular plates and shells,” *Eur. J. Mech. A/Solids* **28**, 500–515 (2009).
- ¹⁶C. Touzé, O. Thomas, and A. Chaigne, “Asymmetric non-linear forced vibrations of free-edge circular plates, Part I: Theory,” *J. Sound Vib.* **258**(4), 649–676 (2002).
- ¹⁷O. Thomas, C. Touzé, and A. Chaigne, “Non-linear vibrations of free-edge thin spherical shells: Modal interaction rules and 1:1:2 internal resonance,” *Int. J. Solids Struct.* **42**(11–12), 3339–3373 (2005).
- ¹⁸A. H. Nayfeh and D. T. Mook, *Nonlinear Oscillations* (John Wiley & Sons, New York, 1979).
- ¹⁹O. Thomas and S. Bilbao, “Geometrically nonlinear flexural vibrations of plates: In-plane boundary conditions and some symmetry properties,” *J. Sound Vib.* **315**(3), 569–590 (2008).
- ²⁰G. W. Jones and L. Mahadevan, “Optimal control of plates using incompatible strains,” *Nonlinearity* **28**(9), 3153–3174 (2015).
- ²¹V. Denis, A. Pelat, C. Touzé, and F. Gautier, “Improvement of the acoustic black hole effect by using energy transfer due to geometric non-linearity,” *Int. J. Nonlinear Mech.* **94**, 134–145 (2017).
- ²²E. Hairer, C. Lubich, and G. Wanner, *Geometric Numerical Integration: Structure-Preserving Algorithms for Ordinary Differential Equations*, 2nd ed. (Springer, New York, 2006).
- ²³G. L. Ostiguy and S. Sassi, “Effects of initial imperfections on dynamic behaviour of rectangular plates,” *Nonlinear Dyn.* **3**, 165–181 (1992).
- ²⁴T. Humbert, O. Cadot, G. Düring, S. Rica, and C. Touzé, “Wave turbulence in vibrating plates: The effect of damping,” *Europhys. Lett.* **102**(3), 30002 (2013).
- ²⁵VK-Gong, “vk-gong [computer program],” <https://vkgong.ensta-paris-tech.fr/> (Last viewed September 4, 2018).
- ²⁶See supplementary material at <https://doi.org/10.1121/1.5091013> for associated sound files in WAV format corresponding to the velocity resampled at 44.1 kHz.
- ²⁷M. Ducceschi, O. Cadot, C. Touzé, and S. Bilbao, “Dynamics of the wave turbulence spectrum in vibrating plates: A numerical investigation using a conservative finite difference scheme,” *Phys. D* **280–281**, 73–85 (2014).
- ²⁸C. Issanchou, J.-L. Le Carrou, C. Touzé, B. Fabre, and O. Doaré, “String/frets contacts in the electric bass sound: Simulations and experiments,” *Appl. Acoust.* **129**, 217–228 (2018).
- ²⁹C. Touzé, O. Thomas, and M. Amabili, “Transition to chaotic vibrations for harmonically forced perfect and imperfect circular plates,” *Int. J. Nonlinear Mech.* **46**(1), 234–246 (2011).
- ³⁰N. H. Fletcher, “Non-linear frequency shifts in quasispherical-cap shells: Pitch glide in Chinese gongs,” *J. Acoust. Soc. Am.* **78**(6), 2069–2071 (1985).
- ³¹C. Touzé, O. Thomas, and A. Chaigne, “Hardening/softening behaviour in non-linear oscillations of structural systems using non-linear normal modes,” *J. Sound Vib.* **273**(1–2), 77–101 (2004).
- ³²M. Jossic, O. Thomas, V. Denis, B. Chomette, A. Mamou-Mani, and D. Roze, “Effects of internal resonances in the pitch glide of Chinese gongs,” *J. Acoust. Soc. Am.* **144**(1), 431–442 (2018).